Materials Science in Semiconductor Processing 31 (2015) 618–623

Contents lists available at ScienceDirect

Materials Science in Semiconductor Processing

journal homepage: www.elsevier.com/locate/mssp

Structural, electronic and optical features of molybdenum-doped bismuth vanadium oxide

V.I. Merupo [a,b], S. Velumani [a,*], G. Oza [a], M. Makowska-Janusik [c], A. Kassiba [b,*]

[a] Departamento de Ingeniería Eléctrica -SEES, CINVESTAV-IPN, Av IPN 2508, Col Zacatenco, D.F. 07360, Mexico
[b] Institute of Molecules & Materials of Le Mans (IMMM) UMR CNRS 6283, Université du Maine, Le Mans, France
[c] Institute of Physics, Jan Dlugosz University in Czestochowa, Al.Armii.Krajowej, 13/15, 42-200 Czestochowa, Poland

ARTICLE INFO

Available online 17 January 2015

Keywords:
Sol–gel
$BiVO_4$
Molybdenum doping
Raman
EPR

ABSTRACT

Molybdenum (Mo)-doped bismuth vanadium oxide ($BiVO_4$) powders were prepared by a sol–gel method. X-ray diffraction (XRD) patterns and micro-Raman vibrational bands confirm the monoclinic scheelite phase. Molybdenum doping of $BiVO_4$ matrix was confirmed from XRD by higher angle 2θ shift of the characteristic peak (-121) and from Raman showing lower frequency shift of dominant band from 831 to 822 cm^{-1} which corresponds to V–O symmetric stretching mode. EPR investigations confirmed the substitution of Mo in the crystalline sites of monoclinic $BiVO_4$. SEM analysis showed spherical shaped particles around 100–200 nm with weak agglomerated particles. Homogeneous presence of molybdenum in $BiVO_4$ matrix was confirmed from STEM analysis. Diffuse reflectance spectra showed higher absorption in the range of 550–850 nm and optical band gap energies were calculated by using the Kubelka–Munk formula, *i.e*, 2.46 eV for 2 wt% Mo–$BiVO_4$ and 2.48 eV for undoped $BiVO_4$. This confirms that, Mo–$BiVO_4$ particles have almost the same energy band gap but induce higher absorption in the visible light region as compared to undoped material.

1. Introduction

Recently, semiconductor photocatalysts have been intensively studied for solving the serious environmental pollution and energy shortage problems. Last two decades, TiO_2 (titanium di-oxide) has been highly investigated photocatalyst because of its low fabrication cost, high photocatalytic efficiency, and high chemical stability in aqueous media [1]. However, TiO_2 with the band gap of 3.2 eV responds only to UV light, which absorbs only ca. 4–6% of the sunlight energy while visible-light accounts for ca. 43% [2]. The search for an efficient visible light driven photocatalyst has led to an upsurge in the field of photocatalysis. Recently, $BiVO_4$ as a visible light driven photocatalyst has received significant attention for water splitting and water detoxification applications [3–5]. Monoclinic scheelite has been considered as more efficient photocatalyst due to its narrow band gap (ca, 2.4–2.5 eV) amongst other phases of $BiVO_4$ such as tetragonal scheelite and tetragonal zircon [6,7]. The main factors required for an efficient semiconductor photocatalyst are the band gap (E_g), the rate of electron–hole generation and the lifetime of excitons. However, there are many other factors which can affect the performance and upsurge efficiency of the photocatalyst, such as depth of penetration of incident light, carrier mobility, effective charge transfer, life span of photo-generated charge carriers (holes and electrons) and their transportation rate from surface of catalyst to solution species [8]. Thus, it is obvious that crystal structure, morphology and composition of photocatalyst play a major role in photocatalysis. Monoclinic scheelite phase is monitored by the energy transition from a valence band being composed

* Corresponding authors.
E-mail addresses: velu@cinvestav.mx (S. Velumani), kassiba@univ-lemans.fr (A. Kassiba).

http://dx.doi.org/10.1016/j.mssp.2014.12.057
1369-8001/

by hybridized orbitals of Bi 6s and O 2p to a conduction band (CB) populated by V 3d orbitals. Thus, it has noticeable band gap reduction ca. ~2.4 eV as compared to other polytypes [9]. However, the photocatalytic behavior of pure $BiVO_4$ is still low due lower mobility of photogenerated charge carriers and shorter diffusion length of carriers which leads to poor charge migration [10]. In general, metal doping can contribute to increase the charge carrier concentration and mobility. Thus, the increment of charge migration as suggested by first principle DFT calculations, contributes to enhance the photoactivity of $BiVO_4$ [11,12].

$BiVO_4$ was modified by doping with transition metals [13–15], rare earth metal [16,17] and noble metals [18–21]. Metal doping contributes significantly to the formation of impurity energy levels inside the band gap. This enhances the promotion of electrons in CB and then the efficiency of photocatalysis. Molybdenum (Mo) and Tungsten (W) has one excess valence electron as compared to Vanadium (V) atom. So, doping of Mo and W could contribute to increase the charge carrier concentration as well as the mobility of photogenerated charges. The photocatalytic efficiency can be then improved in doped $BiVO_4$ [22]. Substitutional Mo doped $BiVO_4$ synthesized by solid state reaction has shown remarkable enhancement in water oxidation and degradation of organic pollutants as reported by Yao et al. [23]. So far, metal doped $BiVO_4$ have been synthesized by several chemical routes, such as co-precipitation [24], sol–gel [25,26] and the impregnation method [14]. However, the sol–gel process is one of the most widely used methods because of easy synthesis, low processing temperature, good control of the composition and better homogeneity of the final solids.

In this report, Mo–$BiVO_4$ was synthesized as powders by using the sol–gel technique with the aim of its applications in the degradation of organic pollutants in aqueous media. XRD and Raman measurements were used to define and reveal the involved crystal structure and the role of Mo doping on the structural features of the samples. Scanning Electron Microscopy (SEM) images shed light on the morphologies and the intimate organization of the material. The location of Mo in monoclinic structure of $BiVO_4$ was investigated by EPR spectroscopy and the results were discussed to point out the dispersion of the doping ions inside the crystal sites. The UV–visible diffuse reflectance spectra features were compared between undoped and Mo-doped $BiVO_4$ samples. The main aim is dedicated to identify the role of Mo doping on the physical features of $BiVO_4$ and the changes of electronic and optical features towards the realization of efficient photocatalyst under visible light irradiation.

2. Experimental procedure

2.1. Synthesis details

Sol–gel synthesis of Mo–$BiVO_4$ powders was done by using 0.01 mol of $Bi(NO_3)_35H_2O$ (> 99.99% trace metals basis, Sigma-Aldrich) dissolved in 50 ml of 10% (w/w) nitric acid to obtain solution A. Similarly, 0.01 mol of NH_4VO_3 (> 99%, ACS reagent, Sigma-Aldrich) was dissolved in 50 ml distilled water at 80 °C to obtain solution B. 0.02 mol citric acid as a chelating agent was added to A and B solutions separately. Solution A was added drop-wise into solution B under vigorous stirring to generate solution C. 2 wt% of molybdenum micro particles (< 150 μm, 99.9%, trace metals basis, Sigma-Aldrich) as dopant were added to 1 ml of NH_4OH to dissolve it completely and then added to solution C. Under vigorous stirring, the pH of mixture was adjusted to approximately 6.5 by using NH_4OH solution. The mixture was stirred at 80 °C until the dark blue sol–gel was obtained, and then the sol–gel was dried for 10 h at 80 °C. The resulting powders were collected, calcinated at 500 °C during 2 h, cooled to room temperature and then crushed to obtain fine powders.

2.2. Characterization techniques

X-ray diffraction patterns of Mo–$BiVO_4$ samples were recorded on an X-ray powder diffractometer (PANanalytical system) which was operated at 40 kV and 35 mA with Cu Kα radiation (α = 1.5418 Å). The morphologies of the samples were observed by using a scanning electron microscope (JEOL, JSM 6510) operating at 20 kV. Micro-Raman measurements were performed using a LabRAM Jobin Yvon spectrometer with a 632.8 nm He–Ne laser source. Electron paramagnetic resonance (EPR) spectra were recorded in X-band (9.4 GHz) at 150 K temperature by using the Bruker EMX spectrometer with cryogenic cryostat from Oxford Instruments. The UV–visible diffuse reflectance spectra were recorded at room temperature with a UV–visible spectrometer (UV-2500, Shimadzu) and converted to an absorbance spectrum by the Kubelka–Munk method.

3. Results and discussion

3.1. X-ray powder diffraction analysis

Crystal structure of Mo–$BiVO_4$ powders were identified by powder X-ray diffraction which show pure monoclinic scheelite phase structure of $BiVO_4$ (JCPDS no. 14-0688) (Fig. 1). The characteristic peaks at $2\theta = 28.8211$ corresponding to (hkl) plane (−121), were slightly shifted (ca. 0.1°) in comparison with undoped $BiVO_4$ shown in inset image of Fig. 1. This shift indicates the occurrence of compressive strains induced in the clinobisvanite system with variation in the lattice dimensions [27] (further justified by Raman analysis in the Section 3.2 and Fig. 2) by the incorporation of molybdenum instead of vanadium in monoclinic structure of $BiVO_4$. This is caused by the ionic radii of V^{5+} (0.050 nm) (in tetrahedral coordination) being close to the substitutional Mo^{6+} (0.055 nm) in the same tetrahedral arrangement [28]. It is well known fact that the lattice exhibits distortions with doping elements into the crystal host sites. Lattice unit cell dimensions and atomic positions were calculated for Mo–$BiVO_4$ and $BiVO_4$ by the Reitveld method using MAUD software. Refined parameters were shown in Table 1 and Table 2 respectively. The compressed unit cell of Mo–$BiVO_4$ is due to the substitution of Mo in few sites of V as reflected from the positional change of V, O_1 and O_2, while Bi did not show any structural change. These data confirmed the substitution of tetrahedral coordinated V by Mo ions in the crystal lattice sites. The crystal domain sizes of Mo–$BiVO_4$ and undoped $BiVO_4$ were 34.5 and 33.8 nm as calculated from Scherrer's formula.

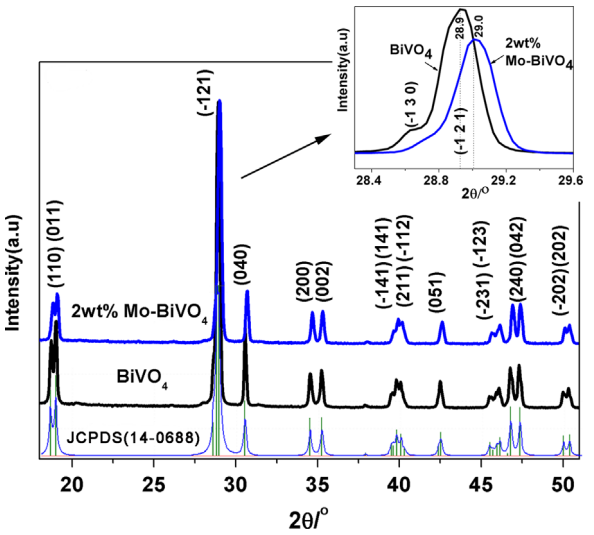

Fig. 1. XRD pattern of Mo–$BiVO_4$ synthesized by the sol–gel method in comparison with undoped $BiVO_4$ along with diffraction pattern of JCPDS no. 14-0688. The inset shows characteristic peak shift to higher angle 2θ position.

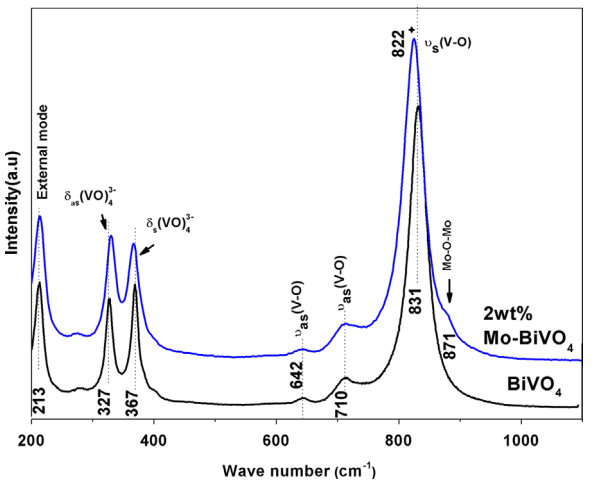

Fig. 2. Raman spectra of 2 wt% Mo–$BiVO_4$ compared to undoped $BiVO_4$.

Table 1
Lattice parameters for monoclinic scheelite phase of $BiVO_4$ without and with Mo doping.

Sample	*a* (Å)	*b* (Å)	*c* (Å)	γ (°)	Volume of cell (10^6 pm^3)
$BiVO_4$	5.195	5.093	11.704	90.38	309.74
2 at% Mo–$BiVO_4$	5.173	5.087	11.661	90.32	307.58

The line broadening was measured by using a standard diffraction pattern of LaB_6 (Lanthanum hexaboride powder). Instrumental broadening measured as 0.046° in 2θ was subtracted from the FWHM observed from diffracted patterns of Mo–$BiVO_4$ powders.

3.2. Raman investigations

Raman spectra showed the same features for both undoped and Mo-doped $BiVO_4$ powders (Fig. 2). The dominant Raman band near ca. 831 cm^{-1} is assigned to stretching modes ν_s(V–O), with a weak shoulder at ca. 710 cm^{-1} which is assigned to ν_{as}(V–O). The $\delta_a(VO_4^{-3})$ and $\delta_{as}(VO_4^{-3})$ modes are around ca. 327 and 367 cm^{-1}. External (rotational/translational) modes are near ca. 213 cm^{-1} [29]. For Mo–$BiVO_4$, the V–O stretching mode has been shifted to a lower wavenumber (822 cm^{-1}) as compared to 831 cm^{-1} for $BiVO_4$. This reveals that the average short-range symmetry of VO_4 tetrahedron becomes more. This shift justifies V–O bond length increment because of the replacement of V by Mo in VO_4 tetrahedron [30,31]. This is also confirmed by the presence of Mo–O–Mo stretching mode at ca. 871 cm^{-1}.

3.3. EPR probing of Mo ions in $BiVO_4$

The fundamental electronic configuration of the molybdenum is [Kr] $4d^5\,5s^1$. The oxidation state of Mo is quite versatile and can be stabilized as Mo^{3+}, Mo^{4+}, Mo^{5+} and Mo^{6+}. EPR spectroscopy is sensitive tool to identify the valence states of Mo through the fine structure of the EPR spectra. However, some valence states as Mo^{4+} and Mo^{6+} cannot be identified because they are spin-less ions and then are EPR silent species. The paramagnetic ions Mo^{3+} ($4d^3$), and Mo^{5+} ($4d^1$) give rise to EPR signals with quite different features since these ions are characterized by effective spins $S=1/2$, 3/2 respectively. As the valance state of V ions is (+5), this should be the expected valence for substitutional Mo ions in the host crystal sites of $BiVO_4$. This situation is indeed involved in Mo-

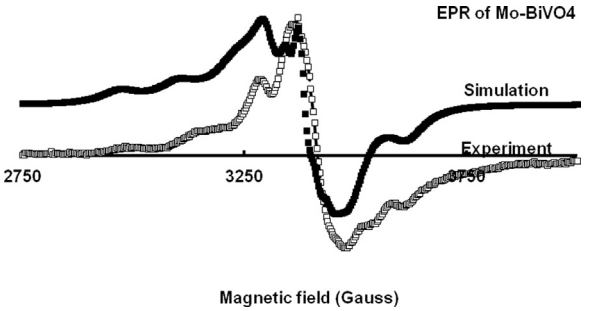

Fig. 3. Electron paramagnetic resonance spectra of Mo^{5+} ions, 2 wt% Mo–$BiVO_4$ powder recorded at 150 K.

Table 2
Atomic positions in undoped and Mo doped monoclinic $BiVO_4$ refined by the Reitveld method.

Sample	Bi	V	O_1	O_2
$BiVO_4$	0, 0.25, 0.6337	0, 0.25, 0.1352	0.149, 0.506, 0.210	0.258, 0.379, 0.451
2 at% Mo–$BiVO_4$	0, 0.25, 0.6275	0.05, 0.255, 0.104	0.121, 0.483, 0.184	0.249, 0.414, 0.450

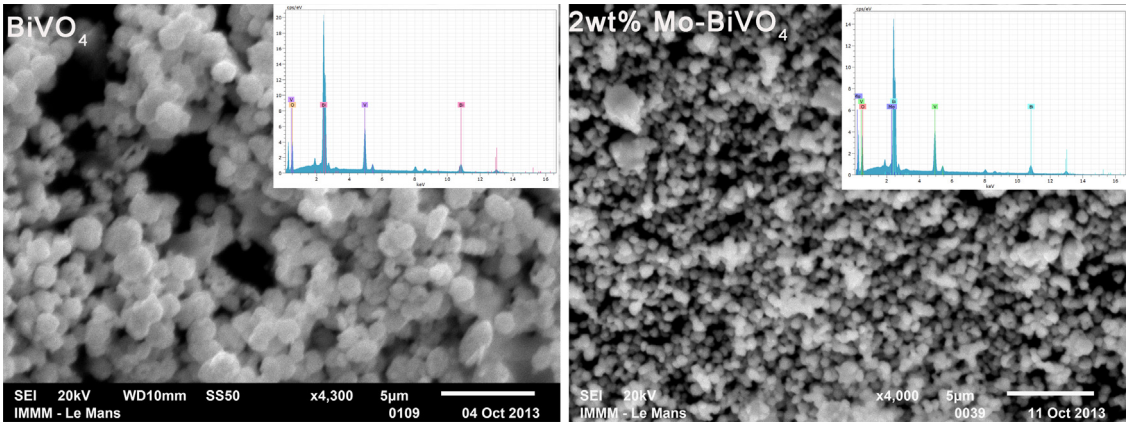

Fig. 4. SEM images of undoped $BiVO_4$ and Mo doped $BiVO_4$ with EDAX composition in inset.

Table 3
Elemental composition of $BiVO_4$ and 2 wt% Mo doped $BiVO_4$ powder samples from EDAX.

Elements	$BiVO_4$	
	Undoped (at%)	2 wt% Mo (at%)
Vanadium	36.19	34.38
Bismuth	28.11	27.39
Oxygen	35.70	36.67
Molybdenum	-	1.06
Total	100	100

doped $BiVO_4$ and the experimental EPR spectrum (Fig. 3) is well accounted by an effective spin $S=1/2$ as for Mo^{5+}. The simulated EPR spectrum was achieved by using $S=1/2$ and the nuclear spin $I=5/2$ related to the natural abundance of ^{95}Mo about (15.92) and of ^{97}Mo about (9.55). The remaining isotopes have no nuclear spin and their spectra did not exhibit any hyperfine splitting. The spectral parameters deduced from the simulation of the EPR spectra which is adjusted by using Bruker commercial software Winsimfonia are $g_x=1.94$, $g_y=1.91$, $g_z=1.99$ and the hyperfine parameters $A_x=30$ Gauss, $A_y=40$ Gauss, $A_z=120$ Gauss. The anisotropy of the spectral parameters underlines the location of Mo^{5+} ions in the crystal sites with orthorhombic local symmetry. This result is consistent with the Raman investigations, which have shown that distortion of the tetrahedrons (VO_4) is due to Mo substitution. Thus, Raman and EPR experiments underline the achievement of Mo substitution inside the crystal sites of $BiVO_4$. These changes will be traduced on the electronic and optical features of Mo–$BiVO_4$.

3.4. Morphological studies

The surface morphology and particle size were determined by SEM for 2 wt% Mo–$BiVO_4$ and undoped $BiVO_4$ samples (Fig. 4). Spherical shapes with submicron sizes are observed for the undoped $BiVO_4$. In contrast, small particles with well-defined shapes are seen for Mo–$BiVO_4$. The different morphologies of undoped and doped samples point out the role of doping in controlling the growth process. Furthermore, the chemical composition of Mo–$BiVO_4$ and $BiVO_4$ samples were performed by EDX analysis and the results are summarized in Table 3. The presence of Mo in doped samples is well ensured in agreement with the above structural and electronic characterizations.

Finally, analysis was made by scanning transmission electron microscopy (STEM) to probe the distribution of chemical constituents in Mo doped samples (Fig. 5).

3.5. Optical features

The typical diffuse reflectance spectra of Mo–$BiVO_4$ and $BiVO_4$ powder samples are shown in Fig. 6. Mo–$BiVO_4$ has shown stronger absorption in visible region (500–850 nm) with slight red-shift of the absorption threshold edge as compared to undoped $BiVO_4$. From the diffuse reflectance spectra, the optical band gap measurements were determined by using approximate formula derived from the Kubelka–Munk model:

$$F(R)=\frac{(1-R)^2}{2R}=\frac{k}{s}=\frac{Ac}{s} \quad (1)$$

where R is the absolute reflectance of the sample, k the molar absorption coefficient, s the scattering coefficient, c the concentration of the absorbing species and A the absorbance.

From inset of Fig. 6, the calculated energy band gaps of $BiVO_4$ and Mo doped $BiVO_4$ are 2.48 eV and 2.46 eV respectively.

The substituted Mo in $BiVO_4$ lattice is expected to form impurity with energy levels formed by hybridization of 4d orbitals of Mo and the 2p orbital of oxygen between the VB and CB. As a consequence changes in the optical absorption are expected from the band edge states induced by bonding and antibonding molecular Mo–O orbitals [28]. Consequently, there is an increment in the optical absorption due to Mo doping, but the shift in the band gap is negligible probably due to low doping rates. However, the effect of the Mo-doping is well traduced on the structural and electronic properties. Tests on the photocatalytic reactions are expected to point out the relevance of Mo

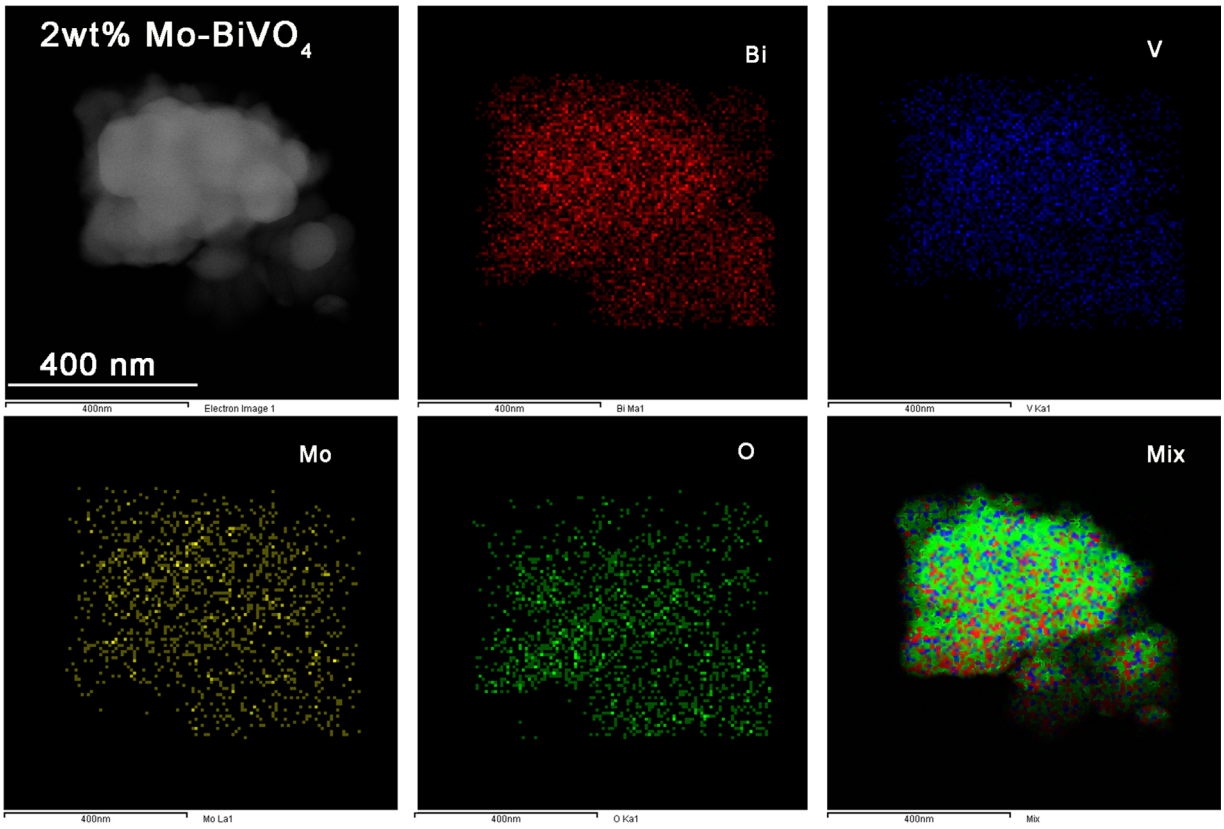

Fig. 5. Elemental distribution probed by STEM analysis of 2 wt% Mo doped $BiVO_4$ samples.

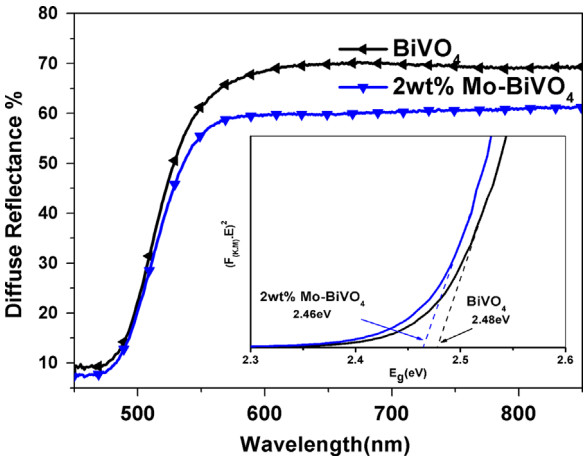

Fig. 6. Diffuse reflectance spectra for undoped and Mo-doped BiVO4. The inset shows the Kubelka–Munk model for the evaluation of the band gap.

doping with respect to undoped $BiVO_4$. These studies are under consideration and will be reported elsewhere.

4. Conclusion

Undoped and Mo doped $BiVO_4$ powders were synthesized by the sol–gel technique. The role of Mo doping on the structural, vibrational, electronic and optical features are investigated by XRD, micro-Raman, EPR and DRS spectroscopy. Although the structure of $BiVO_4$ and Mo–$BiVO_4$ is monoclinic scheelite, moderate structural distortions were observed from the XRD and Raman studies. EPR analysis has shown the achievement of Mo doping through its substitution in the Vanadium crystal sites of $BiVO_4$. This is in agreement with orthorhombic local symmetry of distorted MoO_4 tetrahedrons as suggested from Raman analysis. The optical absorption shows only slight change in the band gap but the rate of absorption is enhanced by Mo doping. The relevance of the Mo doping will be investigated from the photocatalytic activity and its efficiency with respect to undoped $BiVO_4$ sample.

Acknowledgment

The authors are grateful to the Cinvestav-IPN and the Université du Maine for their financial support in the frame of collaborative project 2012–2014. V. Merupo is thankful to the doctoral school 3MPL of the region Pays de la Loire for the financial support in the frame of PhD co-graduation between CINVESTAV-Mexico and Université du Maine. The authors are thankful to Eng. Alvaro Angeles Pascual for STEM analysis.

References

[1] M. Maitani, K. Tanaka, D. Mochizuki, Y. Wada, J. Phys. Chem. Lett. 2 (2011) 265.

[2] D.L. Liao, B.Q. Liao, J. Photochem. Photobiol. A: Chem. 187 (2007) 363.
[3] R. Venkatesan, S. Velumani, A. Kassiba, Mat. Chem. Phys. 135 (2–3) (2012) 842.
[4] A. Kudo, Y. Miseki, Chem. Soc. Rev. 38 (2009) 253.
[5] R. Venkatesan, S. Velumani, M. Tabellout, N. Errien, A. Kassiba, J. Phys. Chem. Sol. 74 (2013) 1695.
[6] H. Jiang, H. Dai, X. Meng, L. Zhang, J. Deng, K. Ji, Chin. J. Catal. 32 (2011) 939.
[7] A. Walsh, Y. Yan, M.N. Huda, M.M. Al-Jassim, S.H. Wei, Chem. Mater. 21 (2009) 547.
[8] H.S. Park, K.E. Kweon, H. Ye, E. Paek, G.S. Hwang, A.J. Bard, J. Phys. Chem. C 115 (2011) 17870.
[9] G.P. Nagabhushana, G. Nagaraju, G.T. Chandrappa, J. Mater. Chem. A 1 (2013) 388.
[10] M. Long, W. Cai, J. Cai, B. Zhou, X. Chai, Y. Wu, J. Phys. Chem. B 110 (2006) 20211.
[11] W.J. Yin, S.H. Wei, M.M. Al-Jassim, J. Turner, Y. Yan, Phys. Rev. B 83 (2011) 155102.
[12] Z. Zhao, Z. Li, Z. Zou, Phys. Chem. Chem. Phys. 13 (2011) 4746.
[13] H. Xu, H. Li, C. Wu, J. Chu, Y. Yan, H. Shu, Mat. Sc. Eng. B 147 (2008) 52.
[14] H. Xu, H. Li, C. Wu, J. Chu, Y. Yan, H. Shu, Z. Gu, J. Hazard. Mat. 153 (2008) 877.
[15] B. Zhou, X. Zhao, H. Liu, J. Qu, C.P. Huang, Appl. Cat.B: Environmental 99 (2010) 214.
[16] M.C. Nevesa, M. Lehockyc, R. Soaresb, L. Lapcik, T. Trindade, Dyes and Pigments 59 (2003) 181.
[17] H. Xu, C. Wua, H. Li, J. Chu, G. Sun, Y. Xu, Y. Yan, Appl. Surf. Sci. 256 (2009) 597.
[18] S. Kohtani, J. Hiro, N. Yamamoto, A. Kudo, K. Tokumura, R. Nakagaki, Catal. Commu. 6 (2005) 185.
[19] X. Zhang, Y. Zhang, X. Quan, S. Chen, J. Hazard. Mater. 167 (2009) 911.
[20] L. Ge, J. Mol. Catal. A: Chem. 282 (2008) 62.
[21] L. Ge, Mat.Lett. 62 (2008) 926.
[22] S.P. Berglund, A.J.E. Rettie, S. Hoang, C.B. Mullins, Phys. Chem. Chem. Phys. 14 (2012) 7065.
[23] W. Yao, H. Iwai, J. Ye, Dalton Trans. 11 (2008) 1426.
[24] H.W. Jeong, T.H. Jeon, J.S. Jang, W. Choi, H. Park, J. Phys. Chem. C 117 (2013) 9104.
[25] M. Wang, H. Zheng, Q. Liu, C. Niu, Y. Che, M. Dang, Spectrochim. Acta Part A: Mol. Biomol. Spectrosc. 114 (2013) 74.
[26] M. Wang, Q. Liu, Y. Che, D. Zhang, J. Alloy compd. 548 (2013) 70.
[27] Y. Yang, Q. Zhang, B. Zhang, W.B. Mi, L. Chen, L. Li, C. Zhao, E.M. Diallo, X.X. Zhang, Appl.Surf.Sci. 258 (2012) 4532.
[28] K. Ding, B. Chen, Z. Fang, Y. Zhang, Z. Chen, Phys. Chem. Chem. Phys. 16 (2014) 13465.
[29] L. Sandhya Kumari, P.Prabhakar Rao, Solar Energy Mater. Solar Cells 112 (2013) 134.
[30] J. Yu, A. Kudo, Adv. Funct. Mater. 16 (2006) 2163.
[31] S.M. Thalluri, C.M. Suarez, M. Hussain, S. Hernandez, A. Virga, G. Saracco, N. Russo, Ind. Eng. Chem. Res. 52 (2013) 17414.